GEOPHYSICS, VOL. 86, NO. 5 (SEPTEMBER-OCTOBER 2021); P. P49–P60, 9 FIGS.
10.1190/GEO2021-0031.1

Near-field strain in distributed acoustic sensing-based microseismic observation

Bin Luo[1], Ge Jin[2], and Frantisek Stanek[2]

ABSTRACT

Microseismic monitoring with surface or downhole geophone arrays has commonly been used in tracking subsurface deformation and fracture networks during hydraulic fracturing operations. Recently, the use of fiber-optic distributed acoustic sensing (DAS) technology has improved microseismic acquisition to a new level with unprecedentedly high spatial resolution and low cost. Deploying fiber-optic cables in horizontal boreholes allows for very close observation of these microsize earthquakes and captures their full wavefield details. We have found that DAS-based microseismic profiles present a seldomly reported near-field strain signal between the P- and S-wave arrivals. This near-field signal indicates a monotonically increasing (or decreasing) temporal variation, which resembles the previously reported near-field observations of large earthquakes. To understand the near-field strain behavior, we use a mathematical expression of the analytic normal strain solution that reveals the near-field, intermediate-near-field, intermediate-far-field, and far-field components. Synthetic DAS strain records of hydraulic-fracture-induced microseismic events can be generated using this analytic solution with the Brune source model. The polarity sign patterns of the near-field and far-field terms in these synthetics are linked to the corresponding source mechanism's radiation patterns. These polarity sign patterns are demonstrated to be sensitive to the source orientations by rotating the moment tensor in different directions. A field data example is compared to the synthetic result, and a qualitative match is shown. The microseismic near-field signals detected by DAS have potential value in hydraulic fracture monitoring by providing a means to better constrain microseismic source parameters that characterize the source magnitude, source orientation, and temporal source evolution and therefore better reflect the geomechanical response of the hydraulically fractured environment in the unconventional reservoirs.

INTRODUCTION

Microseismic monitoring has been used for decades as a powerful tool for monitoring subsurface industrial activities, such as mining, waste fluid injection, and hydraulic fracturing (e.g., Maxwell, 2014). These human activities cause subsurface deformation (e.g., fracturing and faulting) and induce/trigger numerous transient microsize earthquakes that reflect the status of these geomechanical processes. One common application is to use microseismic event locations to map the hydraulic fracture geometry and determine the fracture network properties. The microseismic wavefields, usually P- and S-waves, also can be used to invert for the source mechanism to better constrain the fracture properties (e.g., Vavryčuk, 2007; Eaton and Forouhideh, 2011). These microseismic monitoring techniques have been intensively studied to address safety concerns, stimulation efficiency, and production-related problems.

Microseismic signal acquisition in hydraulic fracturing projects has traditionally been based on either surface arrays (e.g., Duncan and Eisner, 2010) or downhole geophone arrays (e.g., Maxwell et al., 2010). Surface-based monitoring covers large areas with densely distributed sensors, but the sensors are remote from the deep microseismic sources. The radiated seismic signals that can reach the surface arrays are substantially affected by the overburden rock and reservoir depth. However, downhole geophones can be

Manuscript received by the Editor 12 January 2021; revised manuscript received 22 April 2021; published ahead of production 28 May 2021; published online 05 August 2021.
[1]Formerly Colorado School of Mines, Department of Geophysics, Golden, Colorado 80401-1887, USA; presently Stanford University, Geophysics Department, Stanford, California 94305-6104, USA. E-mail: bluo@mines.edu.
[2]Colorado School of Mines, Department of Geophysics, Golden, Colorado 80401-1887, USA. E-mail: gjin@mines.edu (corresponding author); fstanek@mines.edu.

placed close to the microseismic source locations to improve sensitivity, but they are usually sparsely deployed due to high deployment cost and spatially limited downhole environment.

These challenges can be potentially resolved by a recently emerging acquisition technology called distributed acoustic sensing (DAS). DAS is a fiber-optic sensing technology that converts a fiber-optic cable into a densely sampled distributed strain sensor array (Lumens, 2014), which can probe the seismic wavefield with high spatial resolution but yet is sufficiently durable to be installed in the wellbore for close-up observation. DAS has shown great potential in discovering distinct seismic signatures that lead to novel applications in hydraulic fracturing monitoring in tight shale reservoirs, such as scattered waves in time-lapse vertical seismic profiling (e.g., Byerley et al., 2018; Binder et al., 2020; Titov et al., 2020) and low-frequency strain signals in fracture propagation monitoring (e.g., Jin and Roy, 2017; Hull et al., 2019), as well as microseismic S-wave splitting (Baird et al., 2020) and guided waves (e.g., Lellouch et al., 2019; Huff et al., 2020; Luo et al., 2021).

The downhole deployment of a fiber-optic cable near the microseismic events provides high-quality acquisition of a large aperture of microseismic wavefields. Direct P- and S-waves can be identified in the high-resolution DAS seismic profiles (Webster et al., 2013; Karrenbach et al., 2017, 2019; Verdon et al., 2020). Other seismic phases such as converted and reflected body waves due to medium inhomogeneity are also noted as characteristic microseismic features in the DAS profile (Hull et al., 2019). However, these observations are variants of the far-field radiated body waves as they persist long enough to travel through complex structures to reach the stations. A full seismic wavefield emitted from a microseismic event includes additional components, namely, the near-field and the intermediate-field terms, as predicted by the well-studied analytic solution of the displacement field of a moment tensor point source in an infinite homogeneous medium (Aki and Richards, 2002).

Observations of the near-field terms of large earthquakes using surface seismometers and geodetic techniques at short distances have long been reported and used for various applications, such as seismic hazard analysis, source parameter interpretation, and fault-slip inversion (e.g., Aki, 1968; Haskell, 1969; Vidale et al., 1995; Atkinson et al., 2008; Yamada and Mori, 2009; Ruiz et al., 2018; Madariaga et al., 2019). However, these terms are rarely studied in the existing literature of microseismics, partly because they are only observable at short distances (only a few wavelengths) from a microseismic source, which poses a great challenge for either remote surface arrays or sparsely distributed downhole geophone arrays. Nevertheless, thanks to the advent of the DAS technique, high-resolution observation of these near-field waves becomes possible. These waves can be of practical use because they provide additional constraints to the microseismic source mechanism, unlike the commonly used far-field waves that carry incomplete information of the source function and suffer from complex path effects, such as inelastic attenuation, scattering, and multipath interference (Aki and Richards, 2002). Song and Toksöz (2011) propose a full-waveform-based moment tensor inversion algorithm and point out that it is possible to use the full-waveform signal at the near-field range to achieve complete moment tensor inversion even with single-well data. With the first attempt to understand the full wavefield of microseismic events in the context of DAS strain measurements, Vera Rodriguez and Wuestefeld (2020) theoretically extend the analytic expression of the full microseismic wavefield induced by a point source to strain and provide moment tensor inversion resolvability analysis.

In this paper, we examine the near-field strain signals observed in DAS-based microseismic data in horizontal monitor wells. We use the analytic expression of the strain field of a moment tensor point source to provide first-order interpretation of the data in hydraulic-fracturing-related microseismics. Using the theoretical expressions, one can decompose a complicated wavefield into individual elements and understand their behaviors separately. In particular, the expressions provide a means to explain the spatiotemporal variation of the near-field signals as well as the far-field signal. Moreover, we can alter the source orientation in different scenarios and generate synthetics to examine the corresponding radiation patterns of near- and far-field signals in a DAS profile. This study demonstrates that the recorded radiation patterns of the near-field strains along a horizontal DAS cable in the vicinity of a microseismic event are sensitive to the source orientation, and incorporation of this special type of waves in quantitative source inversion can better constrain the moment tensor components.

DATA AND METHOD

Field data processing and observation

We use crosswell DAS data collected during monitoring of a hydraulic fracturing project conducted in the Eagle Ford unconventional reservoir play. In this project, the Eagle Ford layer is the Lower Eagle Ford Shale Formation directly overlain by the Austin Chalk Formation and underlain by the Buda Limestone Formation. A treatment well was drilled into the Eagle Ford layer, and a monitor well was drilled into the Austin Chalk. The horizontal sections of the treatment and monitor wells are parallel to each other, offset by 30 m vertically and 200 m laterally. A downhole DAS fiber was installed along the monitor well for seismic acquisition. The channel spacing is 8 m, and the sampling rate is 2000 Hz. The gauge length used for DAS acquisition is 14 m. Microseismic activity was captured by the crosswell fiber-optic cable during 15 stages of hydraulic fracturing operations. Microseismic events were also monitored by a dense surface geophone array, which yields locations, magnitudes, and moment tensor information of the microseismic events after standard industry processing.

The data acquired from the Eagle Ford project are strain rate measurements of the microseismic wavefields. Noise suppression steps are applied to remove the characteristic DAS noises (Ellmauthaler et al., 2017; Binder et al., 2020). These include applying a median filter across neighboring channels to remove optical fading and subtracting the median trace of the vertical DAS section to remove the common-mode noise. We then integrate the strain rate data in time to obtain strain measurements. A 4 Hz high-pass filter is applied to each strain trace to remove low-frequency background noise. We compare the strain rate and strain profiles of an example microseismic record in Figure 1. The direct P- and S-wave signals are clearly visible on a strain rate profile, which provides a rough estimate of event location and distance from the cable by fitting the hyperbolic curves. However, another signal is observed on the strain profile near the apex of the hyperbolic curves between the direct P- and S-wave arrivals, exhibiting a limited lateral extent from the apex and reversal of polarities about the apex. In addition, this interesting signal shows a characteristic feature of a relatively long period with monotonically increasing (or decreasing) amplitude from P- to S-wave arrival.

We interpret this special signal between P- and S-wave arrivals as the near-field signal of the total seismic wavefield emitted from a double-couple microseismic source, as we will show using the analytic expression of the seismic wavefield of a moment tensor point source. The near-field signal is a relatively low-frequency signal that decays rapidly away from the source. This signal is rarely reported in the microseismic literature due to the limitation of downhole observation methods prior to DAS. The fiber-optic cable installed in the deviated wellbore provides a means to make a close-up observation of this phenomenon with high spatial resolution.

Additional microseismic event examples in the data set are presented in Figure 2. Horizontal event locations and focal mechanisms of these events are derived from surface observation. All three selected events (event indices 397, 599, and 712) show a predominant double-couple mechanism with a nearly vertical nodal plane, implying a shearing nature for these events, either dip slip on induced vertical hydraulic fractures or horizontal slip on a bedding plane (Staněk and Eisner, 2017). Event 599 shows a reversed beach ball polarity compared with the other two, suggesting an opposite slip direction on the fault plane. Comparisons of the DAS waveforms from two near-offset channels symmetric about the apices of the P- and S-wave arrival hyperbola for each of the three selected events are shown in Figure 2b–2d. The P-wave signals are barely observed at these channels due to the near-vertical incident angle. The P-wave arrival times at these channels (approximately 0.04 s from the event origin) are extrapolated from the hyperbolic P-wave arrivals at farther offset. On the contrary, S-wave pulses are significant and are estimated to be approximately 0.075 s from the event origin. Provided a roughly 200 m horizontal separation of these events from the DAS monitor well and neglecting the vertical and well-parallel offsets, the P- and S-wave velocity can be roughly estimated as 5100 and 2700 m/s from their arrivals, respectively. These velocity estimates are close to the velocities of the Austin Chalk above the Eagle Ford according to a sonic log obtained from a nearby vertical well, suggesting that the raypaths of the direct body waves are mainly inside the Austin Chalk layer. In the window between the P- and S-wave arrivals, all of the trace pairs show a monotonic increase in one trace and a monotonic decrease in the other, starting from the estimated P-wave arrivals and ending at the S-wave arrivals. The reversed focal mechanism of event 599 among the three events also presents a reversed polarity of the traces compared with those of the other two example events.

Analytic solution of displacement and strain

Microseismic events are commonly considered to be the result of transient movements along induced or natural fractures and are typically approximated as point sources with their orientations described by moment tensors. They are generally double-couple

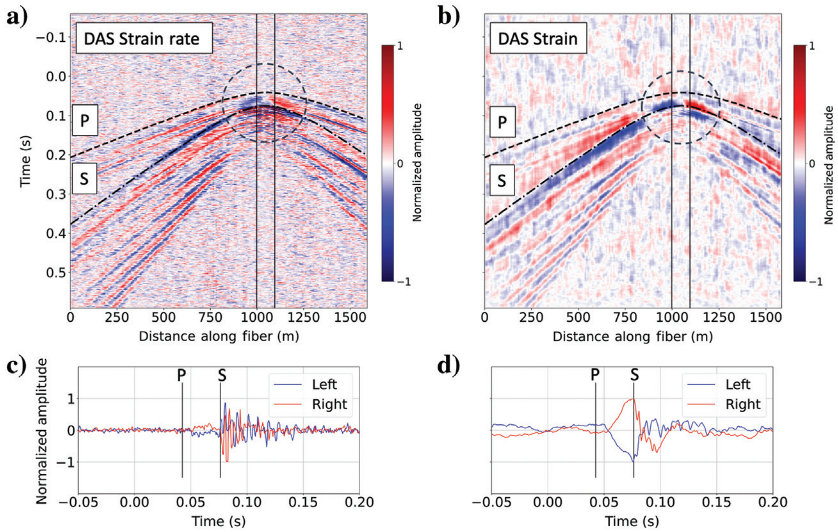

Figure 1. (a and b) The normalized strain rate and strain profiles, respectively, of a microseismic event detected by the horizontal section of the fiber in the monitor well. Direct P- and S-wave arrivals are marked by the dashed curves. The near-field signal near the apex between P- and S-wave arrivals is highlighted by a dashed circle. Two channels symmetric about the apex in (a and b) are marked by the vertical black lines, and data are displayed in (c and d), respectively, for comparison.

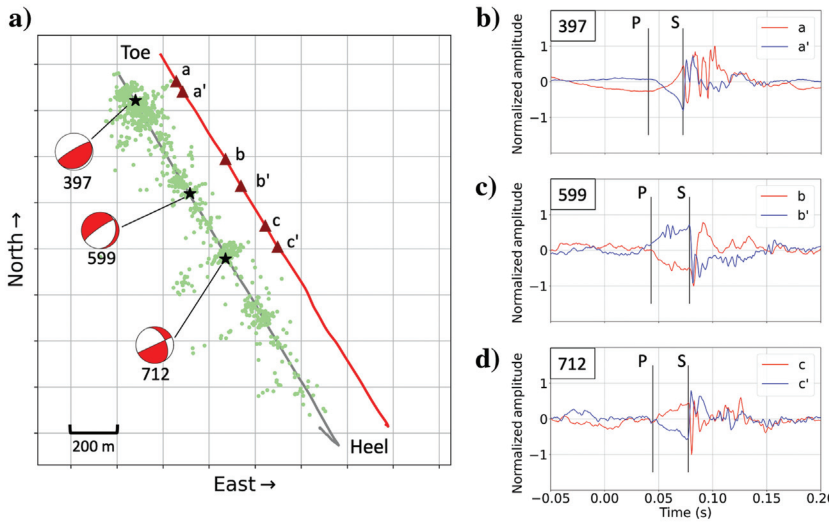

Figure 2. (a) Plan view of microseismic event distribution (the green dots) of the Eagle Ford project. Three microseismic events are selected and highlighted by the black stars. Their focal mechanisms acquired from the surface array are shown by the beach balls, under which the event indices are labeled. The gray and red curves denote the treatment well and DAS monitor well trajectories, respectively. Red triangles on the monitor well denote the selected DAS channels for waveform comparison. (b-d) DAS strain waveform comparison of the selected near-offset channel pairs for each selected microseismic event in (a). Traces are normalized between each channel pair. The origin of the time axis is set to the corresponding event origin.

sources represented by shearing components in the moment tensor (e.g., Rutledge et al., 2004; Maxwell, 2014; Staněk and Eisner, 2017), although isotropic and compensated linear vector dipole (CLVD) components can also come into play in the hydraulic fracturing environment (e.g., Baig and Urbancic, 2010; Song and Toksöz, 2011; Grechka and Heigl, 2017). The expression of the displacement field of a moment tensor point source in a homogeneous isotropic medium can be deduced analytically by convolving the first derivative of the analytic Green's functions of the elastic wave equation with the time-varying function of the moment tensor point source (Aki and Richards, 2002). Here, we briefly summarize the basic properties of the analytic expression. The displacement generated by a moment tensor point source M_{jk} in a homogeneous, isotropic elastic medium consists of five terms: the near field, the intermediate field for P-waves, the intermediate field for S-waves, the far field for P-waves, and the far field for S-waves (Aki and Richards, 2002; Madariaga et al., 2019). Assuming a constant medium with density ρ, P-wave velocity V_{P}, and S-wave velocity V_{S}, the displacement field can be expressed as

$$
\begin{aligned}
u_i(\mathbf{r},t) = & \frac{1}{4\pi\rho}\frac{A^{N}}{r^4}\int_{r/V_{\mathrm{P}}}^{r/V_{\mathrm{S}}}\tau M_{jk}(t-\tau)d\tau + \frac{1}{4\pi\rho V_{\mathrm{P}}^2}\frac{A^{\mathrm{IP}}}{r^2}M_{jk}\left(t-\frac{r}{V_{\mathrm{P}}}\right) \\
& + \frac{1}{4\pi\rho V_{\mathrm{S}}^2}\frac{A^{\mathrm{IS}}}{r^2}M_{jk}\left(t-\frac{r}{V_{\mathrm{S}}}\right) + \frac{1}{4\pi\rho V_{\mathrm{P}}^3}\frac{A^{\mathrm{FP}}}{r}\dot{M}_{jk}\left(t-\frac{r}{V_{\mathrm{P}}}\right) \\
& + \frac{1}{4\pi\rho V_{\mathrm{S}}^3}\frac{A^{\mathrm{FS}}}{r}\dot{M}_{jk}\left(t-\frac{r}{V_{\mathrm{S}}}\right), \qquad (1)
\end{aligned}
$$

where $\mathbf{r}$ is the vector pointing from the source to the receiver, $r = |\mathbf{r}|$ is the distance between the source and the receiver, and A^{N}, A^{IP}, A^{IS}, A^{FP}, and A^{FS} are the radiation pattern factors of the near-field, intermediate-field P, intermediate-field S, far-field P, and far-field S, respectively. The explicit expressions of these radiation patterns are provided in Appendix A. Note that the summation convention is implied for indices j and k. Each of the five individual terms describes three major characteristics of the corresponding wavefield: (1) geometric spreading, which is the negative power function of the source-receiver distance and defines the near-, intermediate-, and far-field terms, (2) the radiation pattern, which determines the directional dependence of the magnitude and the polarity sign of the radiated seismic wavefields, and (3) temporal variation, which describes how the radiated temporal waveforms relate to the time-varying source excitation. This analytic expression provides a first-order insight on the essential constituents of the seismic wavefields radiated from a moment tensor point source that represents a microseismic event.

Although the particle displacement or velocity expression is sufficient for traditional nodal sensors such as geophones, the fiber-optic DAS device measures the strain or strain rate of the seismic wavefields in the form of differential displacement or differential velocity over a finite length. The DAS strain rate and geophone velocity relation has been experimentally verified (Daley et al., 2016; Wang et al., 2018), and the finite length is commonly known as an instrumental parameter of DAS called the gauge length (Lumens, 2014). Therefore, an accurate approximation of the DAS response to the seismic wavefields is found by differencing the displacements at two points separated by a gauge length (Daley et al., 2016; Wang et al., 2018; Binder et al., 2020). To generate synthetic DAS strain measurements, the synthetic displacements at the two points are first evaluated according to the analytic displacement solution and then converted to the DAS strain at the middle of the two points by a finite-difference operation. We follow this scheme to generate synthetic DAS strains, which avoids explicitly considering the directional sensitivity and gauge length effect of the DAS sensors.

A point-sensor approximation may apply when the gauge length is shorter than at least half of the wavelength of the seismic wavefield of interest (Martin, 2018). In this case, infinitesimal strain is derived as the spatial derivative of the particle displacement field. Vera Rodriguez and Wuestefeld (2020) show that the spatial derivative of each term in the displacement solution results in two terms in the strain solution: One is the spatial derivative of the lump of geometric spreading and radiation pattern, and the other is the spatial derivative of the temporal waveform. We briefly summarize this property from their work here. First, it is typically assumed that all nine components of a moment tensor follow the same time variation as a result of the source process (e.g., Vera Rodriguez and Wuestefeld, 2020), i.e., the time-varying moment tensor $M_{jk}(t)$ is given by $M_{jk}(t) = M_{jk}S(t)$, where M_{jk} is a time-invariant moment tensor and $S(t)$ is a scalar time-varying function. Second, for the sake of simplicity, we denote the lumped product of the geometric spreading factor, the radiation pattern factor, and the time-invariant moment tensor by $\mathbf{R}(\mathbf{r})$, which is a vector-valued function of the source-receiver distance vector $\mathbf{r}$. The propagation of the waveform $S(t)$ from the point source to location $\mathbf{r}$ is denoted by $S(t-r/c)$, with $r = |\mathbf{r}|$ and c being either P- or S-wave velocities. Supposing that the DAS cable is oriented in the x-direction, the individual terms of the displacement solution along the cable can be written generically as $u_x = R_x(\mathbf{r})S(t-r/c)$, and the normal strain along the cable can be expressed as

$$
\varepsilon_{xx}(\mathbf{r},t) = \frac{\partial R_x(\mathbf{r})}{\partial x}S\left(t-\frac{r}{c}\right) - \frac{x}{cr}R_x(\mathbf{r})\dot{S}\left(t-\frac{r}{c}\right), \qquad (2)
$$

in which the first term has a new radiation pattern $\partial R_x(\mathbf{r})/\partial x$ with the original wave propagation function $S(t-r/c)$, whereas the second term has a slightly modified radiation pattern $-(x/cr)R_x(\mathbf{r})$ with a temporal derivative of the wave propagation factor $\dot{S}(t-r/c)$. Here, we explicitly write out $\partial S(t-r/c)/\partial x$ in the second term as $-(x/cr)\dot{S}(t-r/c)$, whereas in Vera Rodriguez and Wuestefeld (2020) this derivative is written as the difference quotient of $S(t-r/c)$ with respect to x. The physics in our explicit expression is more straightforward because $-(x/cr)$ is equal to the apparent slowness (whose inverse is the apparent velocity) and serves as the coefficient to convert velocity to DAS axial strain (Lindsey et al., 2020). It also permits combining the like terms in the final expression as we discuss later. The first term, as demonstrated by Vera Rodriguez and Wuestefeld (2020), has a higher negative power on r than the second term and falls to a shorter range propagation. Following the logic of equation 2, the four terms of the intermediate-field and far-field in equation 1 turn into eight terms in the analytic strain solution. The near-field term is an exception with a $\int_{r/V_{\mathrm{P}}}^{r/V_{\mathrm{S}}}\tau M(t-\tau)d\tau$ factor, which splits into two terms when a spatial derivative operation is applied. Therefore, the spatial derivative of the near-field terms has three terms instead of two, and the final analytic normal strain solution has a total of 11 individual terms (see equation A-6 in Appendix A). The like terms can be further combined to yield a concise expression of the normal strain solution with seven individual terms as

$$\begin{aligned}\varepsilon_{ii}(\mathbf{r},t) &= \frac{1}{4\pi\rho}\frac{B^N}{r^5}\int_{r/V_\mathrm{P}}^{r/V_\mathrm{S}}\tau M_{jk}(t-\tau)d\tau + \frac{1}{4\pi\rho V_\mathrm{P}^2}\frac{B^\mathrm{INP}}{r^3}M_{jk}\left(t-\frac{r}{V_\mathrm{P}}\right)\\ &+\frac{1}{4\pi\rho V_\mathrm{S}^2}\frac{B^\mathrm{INS}}{r^3}M_{jk}\left(t-\frac{r}{V_\mathrm{S}}\right)+\frac{1}{4\pi\rho V_\mathrm{P}^3}\frac{B^\mathrm{IFP}}{r^2}\dot{M}_{jk}\left(t-\frac{r}{V_\mathrm{P}}\right)\\ &+\frac{1}{4\pi\rho V_\mathrm{S}^3}\frac{B^\mathrm{IFS}}{r^2}\dot{M}_{jk}\left(t-\frac{r}{V_\mathrm{S}}\right)+\frac{1}{4\pi\rho V_\mathrm{P}^4}\frac{B^\mathrm{FP}}{r}\ddot{M}_{jk}\left(t-\frac{r}{V_\mathrm{P}}\right)\\ &+\frac{1}{4\pi\rho V_\mathrm{S}^4}\frac{B^\mathrm{FS}}{r}\ddot{M}_{jk}\left(t-\frac{r}{V_\mathrm{S}}\right),\end{aligned} \tag{3}$$

where $B^N = A^{N*}$, $B^\mathrm{INP} = A^{\mathrm{IP}*} - \gamma_i A^N$, $B^\mathrm{INS} = A^{\mathrm{IS}*} + \gamma_i A^N$, $B^\mathrm{IFP} = A^{\mathrm{FP}*} - \gamma_i A^\mathrm{IP}$, $B^\mathrm{IFS} = A^{F*} - \gamma_i A^\mathrm{IS}$, $B^\mathrm{FP} = -\gamma_i A^\mathrm{FP}$, and $B^\mathrm{FS} = -\gamma_i A^\mathrm{FS}$. See Appendix A for explicit definitions of A^{N*}, $A^{\mathrm{IP}*}$, $A^{\mathrm{IS}*}$, $A^{\mathrm{FP}*}$, and $A^{\mathrm{FS}*}$. Note that the summation convention applies for subscripts j and k, but not for i because the double i indicates the normal strain component in the x_i direction.

Equation 3 shows a similar structure of the analytic strain solution to the displacement solution 1. Both show a near-field term (NF) and two far-field terms (FP and FS), although the near-field strain attenuates as r^{-5} as opposed to r^{-4} for the near-field displacement, and the far-field strains are proportional to $\ddot{M}_{jk}(t-r/c)$ as opposed to $\dot{M}_{jk}(t-r/c)$ for the far-field displacements. In addition, the intermediate-field strains consist of a total of four terms instead of two as in the displacement solution. According to their geometric spreading factors, we categorize these four terms into two types: the intermediate-near field (INF), which attenuates as r^{-3}, and the intermediate-far field (IFF), which attenuates as r^{-2}. From equation A-6 in Appendix A, it is clear that the INF terms are a result of combining part of the spatial derivative of the near-field displacement and part of the spatial derivative of the intermediate-field displacements and that the IFF terms are a result of combining part of the spatial derivative of the intermediate-field displacements and part of the spatial derivative of the far-field displacements. Taking into account the different propagation speeds, these terms are further identified as INP-wave (INP), INS-wave (INS), IFP-wave (IFP), and IFS-wave (IFS).

Note that equation 3 describes the analytic solution for infinitesimal strain and is only a rough approximation for DAS strain signals because the gauge length effect is not considered. For short-wavelength signals compared to the gauge length, this approximation is deteriorated by the gauge length effect in the spectral contents and radiation patterns (Dean et al., 2017; Martin, 2018). To properly convert point strains to DAS strains, one needs to numerically discretize the gauge length by a certain grid size and average the point strains on the grid to approximate the differential displacement over the gauge length. Theoretically speaking, averaging infinitesimal strains and differencing endpoint displacements are mathematically equivalent and the average strain on a discretized gauge length converges to the differential displacement as the grid resolution increases. In practice, directly calculating analytic strain can provide insights into different components of the radiated strain wavefield for in-depth analysis, whereas converting analytic displacements at gauge-length endpoints to DAS strains is a much more efficient way to generate synthetic DAS strain data.

Source time function for microseismic events

The source time function is the releasing rate of the seismic moment at the source point. It is generally described by a transient impulsive signal, of which the integration is a ramp function with a plateau as the total seismic moment. The most commonly used function for microseismic events is the Brune source model (Brune, 1970), which was initially proposed as a representation of a simplified circular crack rupture process involving the physical parameters such as stress drop and rupture dimension. The mathematical form of the Brune source time function is (Madariaga et al., 2019)

$$\dot{M}(t) = M_0\omega_c^2 t e^{-\omega_c t}, \tag{4}$$

where ω_c is the angular corner frequency controlled by the crack radius (Brune, 1970) and M_0 is the seismic moment defined by crack size, slip, and shear strength. Using ω_c and M_0, the stress drop of the shear dislocation can be estimated (e.g., Boore, 2003). The spectral amplitude of the moment rate $\dot{M}(t)$ in the Brune source model is

$$|\dot{M}(\omega)| = \frac{M_0}{1+(\omega/\omega_c)^2}, \tag{5}$$

which represents the characteristic features of a seismic source, including a flat plateau at low frequencies ($\omega < \omega_c$) and an amplitude decaying as ω^{-2} at high frequencies ($\omega > \omega_c$).

The analytic displacement solution of a moment tensor point source shows that the far-field displacement waveforms are directly proportional to $\dot{M}(t)$, which is the general premise for source parameter estimation from the far-field signal spectra. However, the analytic strain solution shows that the far-field strain waveforms are proportional to $\ddot{M}(t)$, the time derivative of $\dot{M}(t)$, which shows their intrinsic relation to the "far-field velocities" and has a spectral behavior of ω^{-1} at high frequencies. It follows that the new IFF term in strain is proportional to $\dot{M}(t)$ and the new INF term is proportional to $M(t)$, similar to the temporal variation of the far-field and intermediate-field terms in displacement. The near-field waveform in strain is also similar to that in displacement, both of which are proportional to the integration $\int_{r/V_\mathrm{P}}^{r/V_\mathrm{S}}\tau M(t-\tau)d\tau$ between the P and S arrivals.

RESULTS

Synthetic displacement and DAS strain

We use the analytic solutions of the wavefield to generate synthetic strains along a horizontal straight fiber-optic cable induced by a given moment tensor point source. The medium is assumed constant with $V_\mathrm{P} = 5100$ m/s, $V_\mathrm{S} = 2750$ m/s, and $\rho = 2650$ kg/m^3. A plan view schematic diagram of the source-receiver configuration is shown in Figure 3a. The fiber-optic cable is located 200 m horizontally away from the source ($d_H = 200$ m in Figure 3a) and 20 m above the source according to the real well trajectories in the Eagle Ford hydraulic fracturing project (Figure 2). The x-direction is along the straight cable, and the z-direction is pointing downward. A pure xz double-couple source (nonzero M_{xz} and M_{zx}) is used, which represents the source orientation with a vertical and a horizontal nodal plane. The values of M_{xz} and M_{zx} are set to 1.26×10^9 N · m, mimicking a hydraulic-fracture-related microseismic event with $M_w = 0$. We choose a 30 Hz corner frequency for the Brune source time function. Synthetic displacements are first computed and then converted to DAS strain using finite difference over a gauge length. The channel spacing and the gauge length are set to 8 and 14 m, respectively. The zero-offset channel is located in the middle of the cable, and the extent of the cable ranges from −400 to 400 m.

Under these model settings, synthetic displacement data are generated through equation 1 (Figure 3b). The displacement data show vanishing far-field P-wave amplitudes near the apex due to the nodal plane of the M_{xz} double-couple and negative P-wave amplitudes on both sides of the profile due to compression toward the negative offset and expansion toward the positive offset. The far-field S-wave signals have a large negative amplitude from −200 to 200 m, corresponding to one of the four lobes of the classic S-wave radiation pattern. Farther beyond this range, the S-wave signals turn positive in sign but their amplitudes are much reduced due to their shallow incident angle. Negative static displacements can be observed after the transient far-field S-wave signals. Signals from the P- to S-wave arrivals are the near-field signals that combine the near-field and the intermediate-field P-wave terms of the displacement solution 1. The signals show a radiation pattern of three lobes: a positive one at the center and two negative ones on the sides.

DAS strain data are generated by subtracting the displacement traces separated by a gauge length (Figure 3c). According to equations 2 and 3, the radiation patterns of the far-field strain signals are those of the far-field displacement terms multiplied by a negative apparent slowness factor $-(1/c) \cdot (x/r)$. Therefore, the far-field P-wave exhibits two lobes with opposite signs, and the far-field S-wave turns into four lobes with an antisymmetric pattern about the zero offset. These radiation patterns are commonly seen in the DAS microseismic data reported in the existing literature (Karrenbach et al., 2019; Baird et al., 2020; Verdon et al., 2020). The near-field signals between the P- and S-waves also show a radiation pattern of four lobes, but the polarity is reversed compared with the far-field S-wave signals. Static strains after the far-field S-wave can also be observed, with a much lower amplitude compared with the other seismic phases.

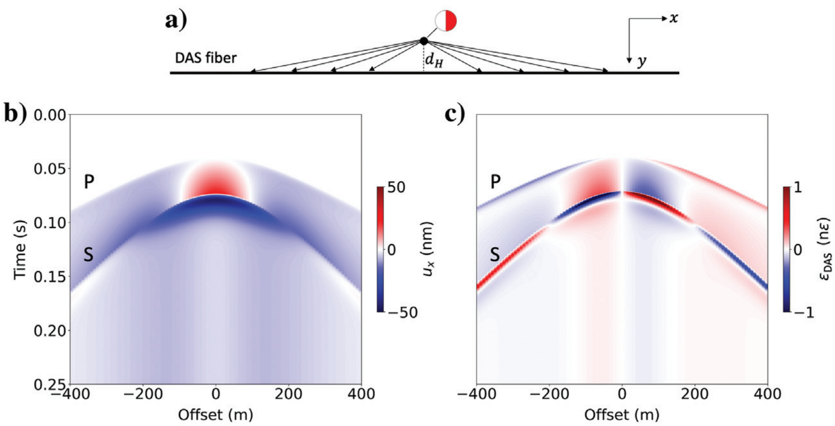

Figure 3. (a) Modeling configuration of a typical hydraulic-fracturing-related double-couple point source. The term d_H is the horizontal distance from the source to the DAS fiber. (b and c) Synthetic u_x profile and DAS strain profile, respectively, along the fiber-optic cable, which is oriented in the x-direction.

The full radiation patterns of the displacement and strain can be evaluated numerically from the radiation pattern factors in equations 1 and 3, respectively. Figure 4 illustrates the radiation patterns of displacement and normal strain in the x-direction. Normal strain is calculated under the point-sensor approximation. Specifically, we calculate the radiation patterns of near-field and far-field terms for displacement and normal strain along the fiber-optic cable because these three terms are predominant features in the synthetic data. Note that according to equation 3 and Appendix A, these strain radiation patterns are related to the displacement ones through $B^{\mathrm{FP}} = -(x/r)A^{\mathrm{FP}}$, $B^{\mathrm{FS}} = -(x/r)A^{\mathrm{FS}}$, and $B^N = r^5(\partial/\partial x)(A^N/r^4)$. Because the fiber-optic cable is placed above the source, it captures the upper half of these radiation patterns. It is obvious that these patterns are consistent with the displacement and strain shown in Figure 3b and 3c.

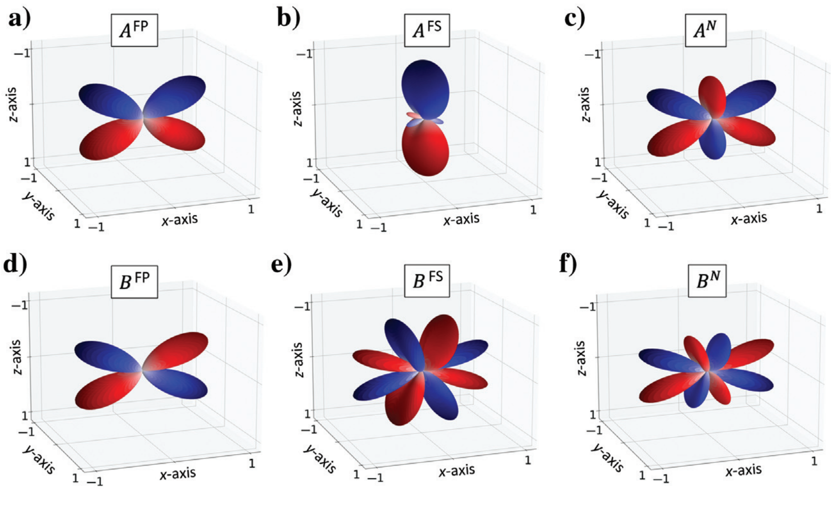

Figure 4. Radiation patterns of an xz double-couple point source. The fiber-optic cable orientation is assumed to be in the x-direction. (a-c) The radiation patterns A^{FP}, A^{FS}, and A^N for displacement u_x, and (d-f) the radiation patterns B^{FP}, B^{FS}, and B^N for normal strain ε_{xx}. The red and blue colors represent the positive and negative signs, respectively.

DAS strain decomposition

It can be numerically verified that averaging point strains from the analytic strain solution 3 generates synthetic DAS data almost identical to those shown in Figure 3c. Synthetic point strains are first computed on a fine grid along the cable and then converted to DAS strains by averaging the synthetic point strains over a gauge length centered at each DAS channel. We tested grid sizes of 1, 0.5, and 0.25 m and their relative root-mean-square differences from the synthetic DAS profile in Figure 3c are 3.5%, 2.2%, and 1.7%, respectively. This allows us to decompose the DAS profile and further analyze the properties of different components of the analytic strain solution 3.

We separately calculate the strain profiles of the near-field, INF, IFF, and far-field strain terms (Figure 5) with the same source mechanism used for the result in Figure 3c. The near-field strain image shows four lobes of different polarity signs along the cable, clearly delineated by the zero-amplitude curves near the 0 and ±200 m offsets (Figure 5a). According to equation 3, the near-field term is a convolution of the moment function $M(t)$ with time between the expected P- and S-wave arrivals, which mainly grows after the P-wave arrival and flattens after the S-wave arrival. After the S-wave arrival, the near-field term reaches a static level that persists over time, as the integral $\int_{r/V_P}^{r/V_S} \tau M(t-\tau)d\tau$ is a constant when $t > r/V_S$.

The INF image (Figure 5b) consists of two parts in time, the INP between P- and S-wave arrivals and a sum of the INP and INS after the S-wave arrival. The INP exhibits the same polarity pattern along the cable as the near-field terms. On the other hand, the INS has a much higher amplitude than the INP and an opposite polarity sign, which therefore reverses the polarity of the profile when it arrives. The INF terms also reach a static strain as the near-field term does due to their proportionality to the ramp function $M(t)$, which reaches a height of M_0 after a finite rise time.

The IFF terms (Figure 5c) and the far-field terms (Figure 5d) are transient signals because they are proportional to the impulsive source time function $\dot{M}(t)$ and its time derivative $\ddot{M}(t)$, respectively. The IFF terms, similar to the near-field term and the INF terms, show four different polarity sections along the cable and opposite polarity between the P- and the S-wave terms.

Summation of all four components yields the total synthetic DAS data (Figure 3c). The transient far-field P- and S-waves are the most prominent features on the image. From the strain decomposition illustrated in Figure 5, the signals between the P- and S-wave arrivals are constructively summed from the near-field, INP, and IFP terms with nearly the same polarity. The static strain after the S-wave arrival, on the other hand, has a relatively low amplitude due to the destructive summation of the near-field term and the INS term.

We select three channels at near-offset, intermediate-offset, and far-offset and present their full waveforms (Figure 6a, 6c, and 6e) and waveform decompositions (Figure 6b, 6d, and 6f). The channels are selected on the positive offset side because the waveforms on the negative side are sign reversed for the simple xz double-couple source. The far-field P- and S-wave arrivals clearly stand out as individual pulses at expected P- and S-wave arrivals, except when their corresponding radiation pattern significantly attenuates the signal, for instance, the trace at the near offset (Figure 6a) barely shows any far-field P-wave signal. For the Brune source model, the $\ddot{M}(t)$ function has a sharp pulse with a high peak followed by a low-amplitude trough. In this simulation, this trough is roughly balanced out by the IFSignals that are in phase with the far-field signals.

A profound feature of the synthetic traces observed in Figure 6 is the monotonically increasing (decreasing) amplitude between the far-field P- and far-field S-wave, which resembles what is observed in the processed microseismic field data (Figures 1d and 2b–2d). For near-offset channels, this feature is the leading signal of the trace as the far-field P is hardly detected due to the poor DAS directional sensitivity to broadside incoming waves. This monotonically growing (declining) signal may be intuitively attributed to the near-field term because this is the only term that preserves the integration function in the strain analytic solution. However, the waveform decomposition shows that it is the synthesis of the near-field term and the INP term. The first half of the monotonically increasing signal is mainly the ramp of the INP, i.e., the ramp of the $M(t)$ function, whereas the second half is dominated by the near-field term, which grows with time. Therefore, this signal may not be explained by one single term in the analytic strain solution. Nonetheless, the near-field and the INP terms are short-range waves that attenuate with distance, and the resultant monotonically growing feature (or declining when the polarity is negative) is therefore a near-field signal that can only be observed at a short distance. Also note that this signal has an opposite polarity to the far-field S-wave signal, which means that, when the far-field S-wave arrives, the trace is predicted to turn sharply to the opposite sign. This feature is also observed in the field data (Figures 1d and 2b–2d).

Effect of moment tensor rotation

The synthetic calculation of the DAS strain profile can be repeated with an arbitrary type of source. Here, we take the previously modeled source mechanism and rotate the strike and the dip angles of the fault plane to examine the radiation pattern registered on the synthetic DAS profile associated with the change of the fault plane orientation.

Figure 7 compares the synthetic data before and after the counterclockwise 20° strike rotation around the z-axis. We can observe an overall change of the polarity patterns of the near-field strain and the far-field S strain toward the side to which the fault strike is reoriented. This is more clearly seen as we trace the polarity-flipping

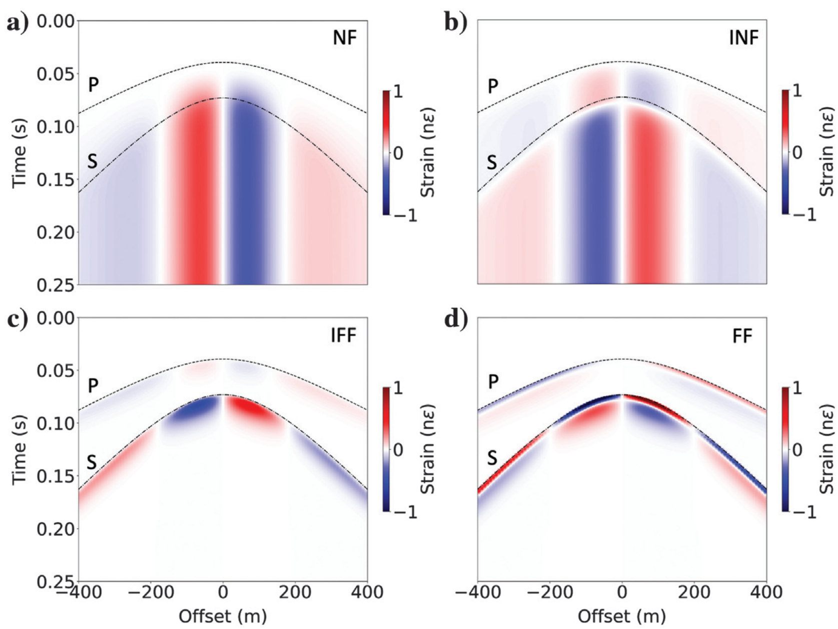

Figure 5. Synthetic DAS strain profiles of the (a) near-field, (b) INF, (c) IFF, and (d) far-field wavefield components. Hyperbolic P and S arrivals are marked with the dotted and dashed-dotted curves, respectively.

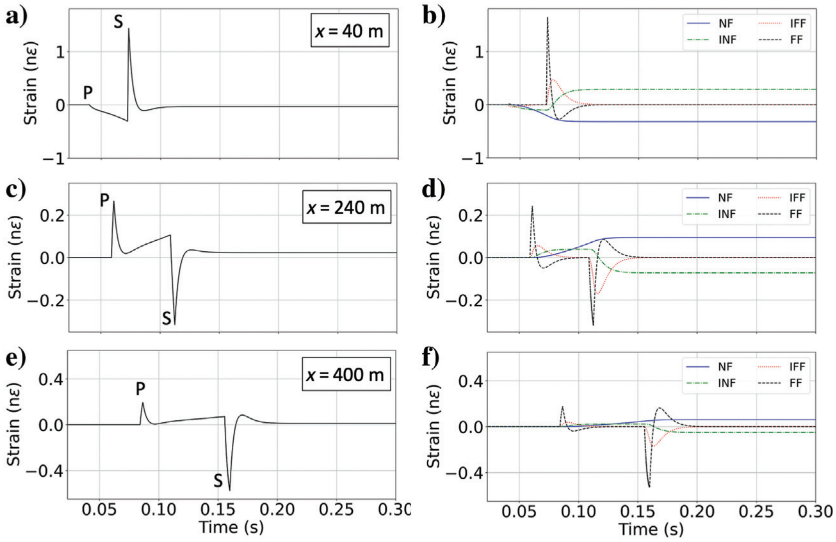

Figure 6. Synthetic full waveforms and waveform decomposition of DAS channels at (a and b) near offset, (c and d) intermediate offset, and (e and f) far offset. NF, INF, IFF, and FF waveforms are shown by the solid blue, dashed-dotted green, dotted red, and dashed black curves, respectively. The P- and S-wave arrivals are marked on the full-waveform traces.

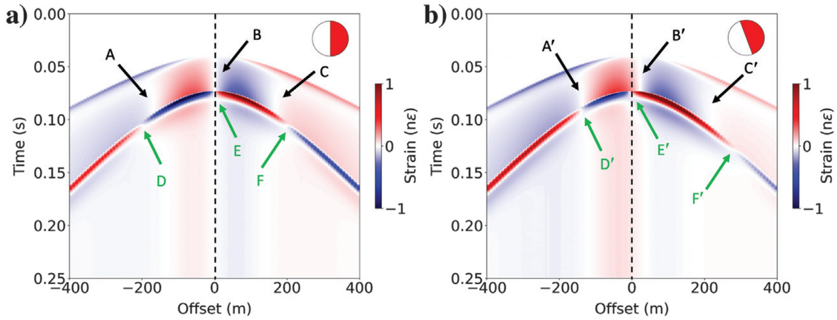

Figure 7. Comparison of the DAS strain synthetics (a) before and (b) after a 20° strike angle rotation of the vertical nodal plane of the double-couple point source. The black and green arrows highlight the polarity-flipping points of the near-field and far-field S amplitudes, respectively.

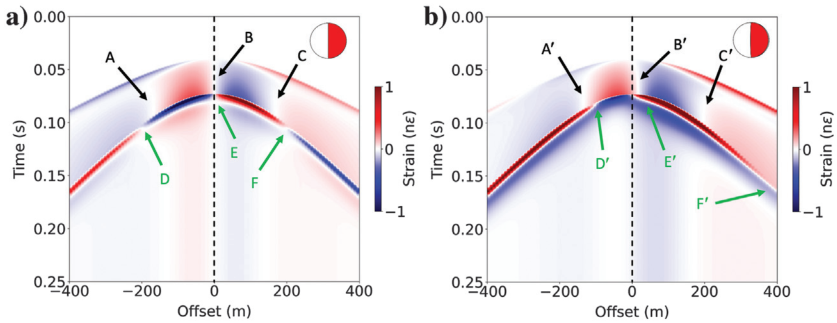

Figure 8. Comparison of the DAS strain synthetics (a) before and (b) after a 4° dip angle rotation of the vertical nodal plane of the double-couple point source. The black and green arrows highlight the strain polarity-flipping points of the near-field and far-field S amplitudes, respectively.

points (marked by the arrows). For the near-field term, all three flipping points (A, B, and C in Figure 7a) move to the right (A′, B′, and C′ in Figure 7b). However, for the far-field S term, two points (D and F in Figure 7a) move to the right (D′ and F′ in Figure 7b), whereas the middle point (E in Figure 7a) stays unmoved (E′ in Figure 7b). This can be clearly explained by the coefficient $-(x/cr)$ in the second term of expression 2, which causes the opposite polarity about the zero offset and is independent of the source orientation. The same explanation holds for far-field P, although the signal has poor sensitivity at the apex. The near-field strain, on the contrary, does not have the unmoved sign-flipping center because it is described by the first term of expression 2.

We can also rotate the fault plane around the y-axis to change the dip angle. We find that this operation can drastically change the polarity pattern even for a slight amount of rotation. The comparison before and after a 4° dip angle change in Figure 8 demonstrates the dramatic change in response to such a small rotation. Again, when we trace the polarity-flipping points of the near-field strain and the far-field S strain, we observe that all points of the near-field strain move to the right, whereas the far-field S has only the left and right polarity-flipping points moving, and the middle point remains at the zero-offset channel. Note that these observations are based on a fixed distance between the source and the cable. The polarity-flipping points may also change their locations along the fiber-optic cable when the horizontal distance and relative depth between the source and the cable change because they are essentially controlled by the radiation pattern determined by the azimuth and take-off angle from the source to the receiver.

Field data example

We compare the microseismic DAS field data example with the corresponding synthetic data (Figure 9), which is calculated using the moment tensor obtained from the surface array data. This focal mechanism has a vertical nodal plane dipping at 88°, with a strike angle oriented at 90° from the fiber-optic cable. We choose a 10 Hz corner frequency estimated from the data for the Brune source spectrum. Overall, we observe a reasonable match between the real and synthetic data in terms of the radiation patterns of the near-field strain signals between the P- and S-wave arrivals and the far-field S signals. The far-field S in the real data profile has a profound asymmetry, which is qualitatively comparable to the synthetic profile, as a consequence of the 2° deviation from the vertical position. However, some disagreements exist, particularly for the near-field strain. The middle sign-flipping point of the near-field strain in the real data (B in Figure 9a) is slightly shifted to the right, and the sign-flipping point on the right (C in Figure 9a) is far from the apex, at x = approximately 300 m. This amount of shifting is not captured by the corresponding points in the synthetic profile (B′ and C′ in Figure 9b).

Several reasons can potentially lead to such an inconsistency between the real and synthetic data. First, although the low-frequency noise has been greatly suppressed and the main polarity features of the near-field strain are observable, the background noise is still at a relatively high level. The picked polarity-flipping points on the DAS strain image may thus be biased. Second, the synthetic calculation using the analytic expression assumes an ideal homogeneous isotropic medium, which does not resemble the real medium in the operation zone. During operations, one side of the induced hydraulic fracture has been stimulated whereas the other side probably remains intact. Such an inhomogeneity, on top of the preexisting fracture/fault networks and the stratified geologic structure, may potentially complicate the wavefield propagation. Third, the moment tensor and event location that we use are estimated from the surface microseismic observations, which are subject to a certain level of uncertainty. In this regard, the misfit to DAS observations may help constrain the moment tensor inversion result. Nevertheless, despite these challenges, the reasonable match between the real and the synthetic has demonstrated the effectiveness of downhole DAS in detecting the near-field strain signal from nearby microseismic events.

DISCUSSION

The theory behind the near-field terms has been well-developed from the elastic wave equation for decades. Yet, most of the reported observations focus on near-field ground motions of large earthquakes due to the stringent observation conditions (requiring a large event magnitude and a small source-receiver distance) and the limited observation approaches (mostly near surface). For microsize earthquakes, detecting the near-field terms is extremely difficult and therefore rarely sought after for practical application. The fast development of DAS, however, has changed the situation by economically feasible deployment of hundreds or thousands of sensors for strain measurements along a borehole in the subsurface. The durable fiber-optic cables can be placed very close to the target area to monitor the microseismicity, and the dense sensor distribution allows for high-resolution acquisition of the full seismic wavefield emitted from microseismic events, which includes the near-field signal. One particular advantage of using fiber-optic cables for near-field signal detection is that the near-offset channels have poor sensitivity to normally impinging far-field P-waves. These longitudinal waves are filtered by the instrumental response and the near-field signals can be clearly observed before the far-field S-wave arrivals, as shown by the synthetic and field data in our study.

A practical use of the near-field signals is to aid in resolving the moment tensors of the microseismic events. Precise determination of the full moment tensor components of microseismic events helps accurately interpret source mechanisms and enables better monitoring of the overall activated fracture network and ultimately more effective rock stimulation to optimize reservoir production. Although in this work we present the synthetics of a typical double-couple source for hydraulic-fracture-related microseismic events, a more general decomposition of a microseismic moment tensor includes double-couple, isotropic, and CLVD components. The latter two are nondouble-couple components that may provide insight into fluid-related fracture opening/closing (Maxwell, 2014; Eyre and van der Baan, 2015), in addition to the predominant shearing described by the double-couple component. Shear-tensile sources can be described by moment tensors where slope angle α is added to the double-couple shearing component (Vavryčuk, 2011).

Moment tensor inversion methods have been developed based on the far-field P- and S-wave terms observed by either surface arrays or downhole arrays, or both (e.g., Vavryčuk, 2007; Eaton and Forouhideh, 2011). However, the acquisition configuration significantly affects the resolvability of the full moment tensor. Vavryčuk (2007) demonstrates that a single 1D array along a vertical borehole using far-field P and S is insufficient to uniquely resolve the six independent components of a moment tensor. Multiwell acquisition is one solution but requires an additional cost in drilling. It is desirable to explore other possibilities for a single-well operation. Grechka et al. (2016) point out that imposing certain physical assumptions to regulate the seismic sources, such as a tensile fracture, may overcome the ambiguity in single-well moment tensor inversion. However, the focal sphere coverage is always poor provided a single linear configuration of receivers. Vera Rodriguez and Wuestefeld (2020) show that resolvability can be improved for a single deviated well when the vertical and deviated sections are used, and DAS makes such an acquisition much easier because the fiber-optic cable is a distributed sensor throughout its entire length. They also explore the possibility of combining far-field and intermediate-field data from a 1D downhole array and show that this combination can improve resolvability by one additional resolvable component. It is worth exploring whether incorporating near-field data, which is clearly observable in the microseismic DAS data as we have shown in this work, can reach a full moment tensor recovery, as Song and Toksöz (2011) suggest that a full-waveform-based inversion of 1D data can achieve full moment tensor inversion.

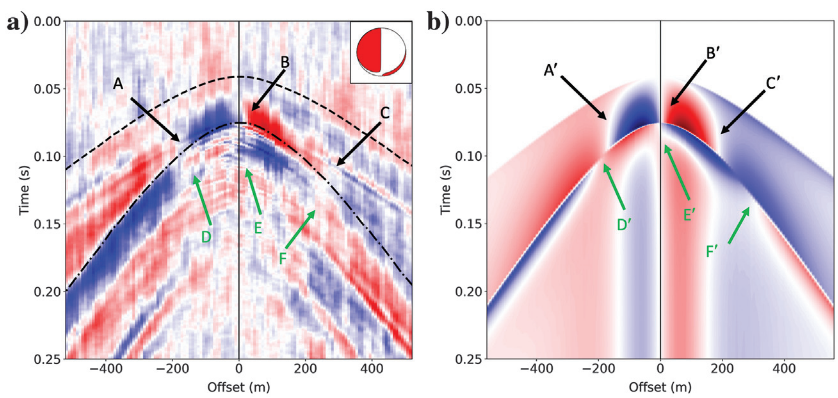

Figure 9. Comparison of (a) the field data of a microseismic event and (b) the synthetic DAS strain profile calculated from the corresponding moment tensor obtained from the surface array. The focal mechanism is shown in the inset of (a). The black and green arrows highlight the strain polarity-flipping points of the near-field signal and far-field S signal, respectively.

The implication of the near-field seismic motions may go further beyond moment tensor inversion because the moment tensor represents equivalent point body force couples in a medium that remains mathematically intact (Burridge and Knopoff, 1964). The near-field seismic motions may also play a key role in resolving details of the fracture geometry and source kinematics. The far-field motions are well known to be the body waves radiating from a local failure; i.e., the dynamic stresses due to the local failure and their spectra usually suffice for source time function retrieval and are used to estimate seismic source attributes such as the seismic moment, source radius, stress drop, and energy release. However, they are inadequate to reveal more information about the source, as demonstrated by Aki and Richards (2002), such that it is necessary to include the near-field motions to completely determine the fault slip kinematics on a finite fault surface. The near-field motions are responses of the static displacements of the local failure, i.e., the static stress changes and permanent strains (push and pull) in the rock matrix due to the new shear fracture. From such a perspective, using the near-field terms may not solely provide the full moment tensor but may also permit reconstruction of the actual shape and dimension of the fracture, which has much practical value in hydraulic fracturing treatments. Another implication of the near-field strain observation may be the crack rupture velocity (V_r), which is typically simplified as a constant parameter in derivation of the corner frequency (e.g., Madariaga, 1976) but may vary considerably in fluid-driven fracture propagation and deformation (e.g., Mizuno et al., 2019). Being able to directly evaluate V_r could allow derivation of more meaningful and interpretable source parameters to diagnose the fracturing process.

Although our analysis is based on the analytic solution of a moment tensor corresponding to a point source pure-shear dislocation, the analysis of near-field signals should be readily extended to a finite fault surface model following the integration over the fault surface deduced by Aki and Richards (2002). In addition, the Green's functions that the analytic solutions are based on may be replaced by numerically derived ones to account for complex geologic structures, such as anisotropic layering and induced fractures. By fitting a total DAS waveform that includes all near-field, intermediate-field, and far-field signals, one can possibly improve the accuracy of traditional source parameter determination as well as reveal a spectrum of source kinematic characteristics. In hydraulic fracturing operations, these details from the microseismic events can be of significant importance for fluid injection effectivity diagnosis and fracture propagation monitoring.

CONCLUSION

We present the microseismic-induced near-field strain signals acquired by the horizontal section of a downhole fiber-optic cable in a deviated well. These signals exhibit monotonically increasing (or decreasing) amplitudes between the P- and S-wave arrivals and a spatially varying polarity pattern. Using the classic analytic displacement solution of a double-couple source in a homogeneous isotropic medium and the Brune source model, we generate DAS strain records of a full wavefield that includes the near-field and far-field signals. We provide a mathematical expression of the analytic normal strain solution that reveals the near-field, intermediate-near-field, intermediate-far-field, and far-field components of the full wavefield and their characteristic properties. The polarity patterns of the near-field and far-field terms in these synthetics are shown to be sensitive to the source mechanism orientations. Qualitative comparison between a field data example and the synthetic result computed for the corresponding moment tensor obtained by the surface array shows reasonable agreement between the two. Incorporating the near-field data into full-waveform-based analysis can potentially help constrain the microseismic source orientation and source parameters and thus shows great value in monitoring future hydraulic fracturing operations.

ACKNOWLEDGMENTS

This work was conducted with the support of the Reservoir Characterization Project at the Colorado School of Mines. The authors are thankful to Devon Energy and Penn Virginia for providing the microseismic DAS data used in this work. Helpful comments from the editors and four reviewers are highly appreciated.

DATA AND MATERIALS AVAILABILITY

Data associated with this research are confidential and cannot be released.

APPENDIX A

ANALYTIC SOLUTION OF DISPLACEMENT AND STRAIN OF A MOMENT TENSOR POINT SOURCE

The displacement generated by a moment tensor point source M_{jk} in a homogeneous, isotropic elastic medium consists of five terms: near-field, intermediate-field P, intermediate-field S, far-field P, and far-field S (Aki and Richards, 2002; Madariaga et al., 2019). Assuming a constant medium with density ρ, P-wave velocity V_P, and S-wave velocity V_S, the displacement field is given in equation 1 in the main text. The radiation pattern factors A^N, A^{IP}, A^{IS}, A^{FP}, and A^{FS}, corresponding to near-field, intermediate-field P, intermediate-field S, far-field P, and far-field S, respectively, are expressed as functions of the directional cosines $\gamma_i = x_i/r$:

$$A^N = 15\gamma_i\gamma_j\gamma_k - 3\delta_{jk}\gamma_i - 3\delta_{ik}\gamma_j - 3\delta_{ij}\gamma_k, \tag{A-1}$$

$$A^{\mathrm{IP}} = 6\gamma_i\gamma_j\gamma_k - \delta_{jk}\gamma_i - \delta_{ik}\gamma_j - \delta_{ij}\gamma_k, \tag{A-2}$$

$$A^{\mathrm{IS}} = -(6\gamma_i\gamma_j\gamma_k - \delta_{jk}\gamma_i - \delta_{ik}\gamma_j - 2\delta_{ij}\gamma_k), \tag{A-3}$$

$$A^{\mathrm{FP}} = \gamma_i\gamma_j\gamma_k, \tag{A-4}$$

$$A^{\mathrm{FS}} = -(\gamma_i\gamma_j\gamma_k - \delta_{ij}\gamma_k), \tag{A-5}$$

where δ_{jk} is the Kronecker delta.

Without a loss of generality, we assume that the fiber-optic cable is oriented in the x_i direction. Therefore, the axial strain along the fiber can be deduced as the normal strain ε_{ii}, which is the spatial derivative of u_i with respect to x_i, expanded following the logic of equation 2:

$$
\begin{aligned}
\varepsilon_{ii}(\mathbf{r},t) = {} & \frac{1}{4\pi\rho}\left[\frac{A^{N*}}{r^5}\int_{r/V_\mathrm{P}}^{r/V_\mathrm{S}}\tau M_{jk}(t-\tau)d\tau + \frac{\gamma_i}{V_\mathrm{S}^2}\frac{A^N}{r^3}M_{jk}\left(t-\frac{r}{V_\mathrm{S}}\right) - \frac{\gamma_i}{V_\mathrm{P}^2}\frac{A^N}{r^3}M_{jk}\left(t-\frac{r}{V_\mathrm{P}}\right)\right] \\
& + \frac{1}{4\pi\rho V_\mathrm{P}^2}\left[\frac{A^{\mathrm{IP}*}}{r^3}M_{jk}\left(t-\frac{r}{V_\mathrm{P}}\right) - \frac{\gamma_i}{V_\mathrm{P}}\frac{A^{\mathrm{IP}}}{r^2}\dot{M}_{jk}\left(t-\frac{r}{V_\mathrm{P}}\right)\right] \\
& + \frac{1}{4\pi\rho V_\mathrm{S}^2}\left[\frac{A^{\mathrm{IS}*}}{r^3}M_{jk}\left(t-\frac{r}{V_\mathrm{S}}\right) - \frac{\gamma_i}{V_\mathrm{S}}\frac{A^{\mathrm{IS}}}{r^2}\dot{M}_{jk}\left(t-\frac{r}{V_\mathrm{S}}\right)\right] \\
& + \frac{1}{4\pi\rho V_\mathrm{P}^3}\left[\frac{A^{\mathrm{FP}*}}{r^2}\dot{M}_{jk}(t-\frac{r}{V_\mathrm{P}}\Big) - \frac{\gamma_i}{V_\mathrm{P}}\frac{A^{\mathrm{FP}}}{r}\ddot{M}_{jk}\left(t-\frac{r}{V_\mathrm{P}}\right)\right] \\
& + \frac{1}{4\pi\rho V_\mathrm{S}^3}\left[\frac{A^{\mathrm{FS}*}}{r^2}\dot{M}_{jk}\left(t-\frac{r}{V_\mathrm{S}}\right) - \frac{\gamma_i}{V_\mathrm{S}}\frac{A^{\mathrm{FS}}}{r}\ddot{M}_{jk}\left(t-\frac{r}{V_\mathrm{S}}\right)\right],
\end{aligned} \tag{A-6}
$$

where the new radiation pattern factors are defined as

$$
\begin{aligned}
A^{N*} = {} & 3[5\gamma_j\gamma_k(1-7\gamma_i^2) + 10(\delta_{ij}\gamma_i\gamma_k + \delta_{ik}\gamma_i\gamma_j) - 2\delta_{ij}\delta_{ik} \\
& - \delta_{jk}(1-5\gamma_i^2)],
\end{aligned} \tag{A-7}
$$

$$
\begin{aligned}
A^{\mathrm{IP}*} = {} & 6\gamma_j\gamma_k(1-5\gamma_i^2) + 9(\delta_{ij}\gamma_i\gamma_k + \delta_{ik}\gamma_i\gamma_j) - 2\delta_{ij}\delta_{ik} \\
& - \delta_{jk}(1-3\gamma_i^2),
\end{aligned} \tag{A-8}
$$

$$
\begin{aligned}
A^{\mathrm{IS}*} = {} & -[6\gamma_j\gamma_k(1-5\gamma_i^2) + (12\delta_{ij}\gamma_i\gamma_k + 9\delta_{ik}\gamma_i\gamma_j) - 3\delta_{ij}\delta_{ik} \\
& - \delta_{jk}(1-3\gamma_i^2)],
\end{aligned} \tag{A-9}
$$

$$
A^{\mathrm{FP}*} = \gamma_j\gamma_k(1-4\gamma_i^2) + \delta_{ij}\gamma_i\gamma_k + \delta_{ik}\gamma_i\gamma_j, \tag{A-10}
$$

$$
A^{\mathrm{FS}*} = -[\gamma_j\gamma_k(1-4\gamma_i^2) + 3\delta_{ij}\gamma_i\gamma_k + \delta_{ik}\gamma_i\gamma_j - \delta_{ij}\delta_{ik}]. \tag{A-11}
$$

Equation A-6 can be reduced to equation 3 by combining the like terms. Similar expressions A-7–A-11 have also been derived by Vera Rodriguez and Wuestefeld (2020) for strain microseismic analysis.

REFERENCES

Aki, K., 1968, Seismic displacements near a fault: Journal of Geophysical Research, **73**, 5359–5376, doi: 10.1029/JB073i016p05359.

Aki, K., and P. G. Richards, 2002, Quantitative seismology: University Science Books.

Atkinson, G. M., S. I. Kaka, D. Eaton, A. Bent, V. Peci, and S. Halchuk, 2008, A very close look at a moderate earthquake near Sudbury, Ontario: Seismological Research Letters, **79**, 119–131, doi: 10.1785/gssrl.79.1.119.

Baig, A., and T. Urbancic, 2010, Microseismic moment tensors: A path to understanding frac growth: The Leading Edge, **29**, 320–324, doi: 10.1190/1.3353729.

Baird, A. F., A. L. Stork, S. A. Horne, G. Naldrett, J.-M. Kendall, J. Wookey, J. P. Verdon, and A. Clarke, 2020, Characteristics of microseismic data recorded by distributed acoustic sensing systems in anisotropic media: Geophysics, **85**, no. 4, KS139–KS147, doi: 10.1190/geo2019-0776.1.

Binder, G., A. Titov, Y. Liu, J. Simmons, A. Tura, G. Byerley, and D. Monk, 2020, Modeling the seismic response of individual hydraulic fracturing stages observed in a time-lapse distributed acoustic sensing vertical seismic profiling survey: Geophysics, **85**, no. 4, T225–T235, doi: 10.1190/geo2019-0819.1.

Boore, D. M., 2003, Simulation of ground motion using the stochastic method: Pure and Applied Geophysics, **160**, 635–676, doi: 10.1007/PL00012553.

Brune, J. N., 1970, Tectonic stress and the spectra of seismic shear waves from earthquakes: Journal of Geophysical Research, **75**, 4997–5009, doi: 10.1029/JB075i026p04997.

Burridge, R., and L. Knopoff, 1964, Body force equivalents for seismic dislocations: Bulletin of the Seismological Society of America, **54**, 1875–1888.

Byerley, G., D. Monk, P. Aaron, and M. Yates, 2018, Time-lapse seismic monitoring of individual hydraulic frac stages using a downhole DAS array: The Leading Edge, **37**, 802–810, doi: 10.1190/tle37110802.1.

Daley, T. M., D. E. Miller, K. Dodds, P. Cook, and B. M. Freifeld, 2016, Field testing of modular borehole monitoring with simultaneous distributed acoustic sensing and geophone vertical seismic profiles at Citronelle, Alabama: Geophysical Prospecting, **64**, 1318–1334, doi: 10.1111/1365-2478.12324.

Dean, T., T. Cuny, and A. H. Hartog, 2017, The effect of gauge length on axially incident P-waves measured using fibre optic distributed vibration sensing: Geophysical Prospecting, **65**, 184–193, doi: 10.1111/1365-2478.12419.

Duncan, P. M., and L. Eisner, 2010, Reservoir characterization using surface microseismic monitoring: Geophysics, **75**, no. 5, 75A139–75A146, doi: 10.1190/1.3467760.

Eaton, D. W., and F. Forouhideh, 2011, Solid angles and the impact of receiver-array geometry on microseismic moment-tensor inversion: Geophysics, **76**, no. 6, WC77–WC85, doi: 10.1190/geo2011-0077.1.

Ellmauthaler, A., M. E. Willis, X. Wu, and M. LeBlanc, 2017, Noise sources in fiber-optic distributed acoustic sensing VSP data: 79th Annual International Conference and Exhibition, EAGE, Extended Abstracts, doi: 10.3997/2214-4609.201700515.

Eyre, T. S., and M. van der Baan, 2015, Overview of moment-tensor inversion of microseismic events: The Leading Edge, **34**, 882–888, doi: 10.1190/tle34080882.1.

Grechka, V., Z. Li, B. Howell, and V. Vavryčuk, 2016, Single-well moment tensor inversion of tensile microseismic events: Geophysics, **81**, no. 6, KS219–KS229, doi: 10.1190/geo2016-0186.1.

Grechka, V. I., and W. M. Heigl, 2017, Microseismic monitoring: SEG.

Haskell, N. A., 1969, Elastic displacements in the near-field of a propagating fault: Bulletin of the Seismological Society of America, **59**, 865–908.

Huff, O., A. Lellouch, B. Luo, G. Jin, and B. Biondi, 2020, Validating the origin of microseismic events in target reservoir using guided waves recorded by DAS: The Leading Edge, **39**, 776–784, doi: 10.1190/tle39110776.1.

Hull, R., R. Meek, H. Bello, K. Woller, and J. Wagner, 2019, Monitoring horizontal well hydraulic stimulations and geomechanical deformation processes in the unconventional shales of the Midland Basin using fiber-based time-lapse VSPs, microseismic, and strain data: The Leading Edge, **38**, 130–137, doi: 10.1190/tle38020130.1.

Jin, G., and B. Roy, 2017, Hydraulic-fracture geometry characterization using low-frequency DAS signal: The Leading Edge, **36**, 975–980, doi: 10.1190/tle36120975.1.

Karrenbach, M., S. Cole, A. Ridge, K. Boone, D. Kahn, J. Rich, K. Silver, and D. Langton, 2019, Fiber-optic distributed acoustic sensing of microseismicity, strain and temperature during hydraulic fracturing: Geophysics, **84**, no. 1, D11–D23, doi: 10.1190/geo2017-0396.1.

Karrenbach, M., D. Kahn, S. Cole, A. Ridge, K. Boone, J. Rich, K. Silver, and D. Langton, 2017, Hydraulic-fracturing-induced strain and microseismic using in situ distributed fiber-optic sensing: The Leading Edge, **36**, 837–844, doi: 10.1190/tle36100837.1.

Lellouch, A., S. Horne, M. A. Meadows, S. Farris, T. Nemeth, and B. Biondi, 2019, DAS observations and modeling of perforation-induced guided waves in a shale reservoir: The Leading Edge, **38**, 858–864, doi: 10.1190/tle38110858.1.

Lindsey, N. J., H. Rademacher, and J. B. Ajo-Franklin, 2020, On the broadband instrument response of fiber-optic DAS arrays: Journal of Geophysical Research, Solid Earth, **125**, e2019JB018145, doi: 10.1029/2019JB018145.

Lumens, P. G. E., 2014, Fibre-optic sensing for application in oil and gas wells: Technische Universiteit Eindhoven.

Luo, B., A. Lellouch, G. Jin, B. Biondi, and J. Simmons, 2021, Seismic inversion of shale reservoir properties using microseismic-induced guided waves recorded by distributed acoustic sensing: Geophysics, **86**, no. 4, R383–R397, doi: 10.1190/geo2020-0607.1.

Madariaga, R., 1976, Dynamics of an expanding circular fault: Bulletin of the Seismological Society of America, **66**, 639–666.

Madariaga, R., S. Ruiz, E. Rivera, F. Leyton, and J. C. Baez, 2019, Near-field spectra of large earthquakes: Pure and Applied Geophysics, **176**, 983–1001, doi: 10.1007/s00024-018-1983-x.

Martin, E. R. L. B.-M., 2018, Passive imaging and characterization of the subsurface with distributed acoustic sensing: Stanford University.

Maxwell, S., 2014, Microseismic imaging of hydraulic fracturing: Improved engineering of unconventional shale reservoirs: SEG.

Maxwell, S. C., J. Rutledge, R. Jones, and M. Fehler, 2010, Petroleum reservoir characterization using downhole microseismic monitoring: Geophysics, **75**, no. 5, 75A129–75A137, doi: 10.1190/1.3477966.

Mizuno, T., J. Le Calvez, and J. Rutledge, 2019, Variation of seismic scalar moment-corner frequency relationship during development of a hydraulic fracture system: The Leading Edge, **38**, 123–129, doi: 10.1190/tle38020123.1.

Ruiz, J. A., E. Contreras-Reyes, F. Ortega-Culaciati, and P. Manríquez, 2018, Rupture process of the April 24, 2017, Mw 6.9 Valparaíso earthquake from the joint inversion of teleseismic body waves and near-field data: Physics of the Earth and Planetary Interiors, **279**, 1–14, doi: 10.1016/j.pepi.2018.03.007.

Rutledge, J. T., W. S. Phillips, and M. J. Mayerhofer, 2004, Faulting induced by forced fluid injection and fluid flow forced by faulting: An interpretation of hydraulic-fracture microseismicity, Carthage Cotton Valley gas field, Texas: Bulletin of the Seismological Society of America, **94**, 1817–1830, doi: 10.1785/012003257.

Song, F., and M. N. Toksöz, 2011, Full-waveform based complete moment tensor inversion and source parameter estimation from downhole microseismic data for hydrofracture monitoring: Geophysics, **76**, no. 6, WC103–WC116, doi: 10.1190/geo2011-0027.1.

Staněk, F., and L. Eisner, 2017, Seismicity induced by hydraulic fracturing in shales: A bedding plane slip model: Journal of Geophysical Research, Solid Earth, **122**, 7912–7926, doi: 10.1002/2017JB014213.

Titov, A., G. Binder, Y. Liu, G. Jin, J. Simmons, A. Tura, D. Monk, G. Byerley, and M. Yates, 2020, Modeling and interpretation of scattered waves in interstage distributed acoustic sensing vertical seismic profiling survey: Geophysics, **86**, no. 2, D93–D102, doi: 10.1190/geo2020-0293.1.

Vavryčuk, V., 2007, On the retrieval of moment tensors from borehole data: Geophysical Prospecting, **55**, 381–391, doi: 10.1111/j.1365-2478.2007.00624.x.

Vavryčuk, V., 2011, Tensile earthquakes: Theory, modeling, and inversion: Journal of Geophysical Research, Solid Earth, **116**, 12320, doi: 10.1029/2011JB008770.

Vera Rodriguez, I., and A. Wuestefeld, 2020, Strain microseismics: Radiation patterns, synthetics, and moment tensor resolvability with distributed acoustic sensing in isotropic media: Geophysics, **85**, no. 3, KS101–KS114, doi: 10.1190/geo2019-0373.1.

Verdon, J. P., S. A. Horne, A. Clarke, A. L. Stork, A. F. Baird, and J.-M. Kendall, 2020, Microseismic monitoring using a fiber-optic distributed acoustic sensor array: Geophysics, **85**, no. 3, KS89–KS99.

Vidale, J. E., S. Goes, and P. G. Richards, 1995, Near-field deformation seen on distant broadband seismograms: Geophysical Research Letters, **22**, 1–4, doi: 10.1029/94GL02893.

Wang, H. F., X. Zeng, D. E. Miller, D. Fratta, K. L. Feigl, C. H. Thurber, and R. J. Mellors, 2018, Ground motion response to an ML 4.3 earthquake using co-located distributed acoustic sensing and seismometer arrays: Geophysical Journal International, **213**, 2020–2036, doi: 10.1093/gji/ggy102.

Webster, P., J. Wall, C. Perkins, and M. Molenaar, 2013, Micro-seismic detection using distributed acoustic sensing: 83rd Annual International Meeting, SEG, Expanded Abstracts, 2459–2463, doi: 10.1190/segam2013-0182.1.

Yamada, M., and J. Mori, 2009, Using τc to estimate magnitude for earthquake early warning and effects of near-field terms: Journal of Geophysical Research, Solid Earth, **114**, B05301, doi: 10.1029/2008JB006080.

Biographies and photographs of the authors are not available.